Fully Lagrangian Approach of Three-Phase Systems for Debris Bed Formation (Part III: External Shape)

YoungWoo Son, InSoo Seo, Cheol-O Ahn*
Metariver Technology Co., Ltd., C-716, Moonjeong-SK-V1, 128, Beobwon-ro, Songpa-gu, Seoul, 05854, Republic of Korea
**Corresponding author: coahn@metariver.kr*

Keywords : DAVINCI experiment, three-phase flow, Discrete Bubble Model (DBM), Moving Particle Semi-implicit (MPS), Discrete Element Method (DEM)

1. Introduction

In a severe LWR (Light-Water Reactor) accident involving core fuel melting, corium released outside the reactor is expected to form a porous debris layer that accumulates at the bottom of the pool. To assess the coolability of this corium debris layer, understanding its formation process and geometrical shape is essential.

Kim et al. [1][2] investigated the external shape of a debris bed affected by two-phase flow induced by vapor generation due to the decay heat of the debris layer using the DAVINCI facility. In this experiment, they injected 5 kg of stainless-steel simulant particles with a diameter and height of 2 mm from the top of the water surface. They injected air bubbles simulating vapor flow from the bottom of the particle catcher plate. The airflow rate was determined based on the quantity of settled debris, which will form a heat source due to the decay of corium. The radial distribution of the settled debris was analyzed using a five-step "gap-tooth" approach. The method they employed used the particle layer generated in the previous step as the initial condition for the next step, with each step designed to drop 1 kg of simulated particles for approximately 10 seconds. Therefore, the experiment, consisting of five stages, allowed for the observation of particle layer formation at each stage by dropping 5 kg of simulated particles over 50 seconds.

The particle column formed by falling particles and the bubble column created by air injection from the bottom each induce opposite flows that collide, resulting in very complex behavior and ultimately causing the particles to scatter downward. A complex flow field results from many bubbles generated by air injection, which alters the particles' settling paths and influences the debris bed formation. Therefore, to accurately predict the shape of the debris layer formed under various conditions, a simulation that considers all interactions between liquid, particle, and bubble is necessary.

Previously, we published two papers [3][4] with the same title, comparing our results with the DAVINCI experiments (internal structure) conducted by Kim et al. and analyzing the influence of debris sphericity. This paper presents the results of a comparison with other experiments (external shape) conducted using the same experimental equipment.

2. DAVINCI experiment

Fig. 1 shows the DAVINCI test facility, which was designed to simulate particulate debris flow in a flooded reactor cavity along with a heat-generating debris bed. The DAVINCI facility consists of three main parts: a particle injection system, a test tank, and a particle catcher plate (PCP) module with an air injection system. The particle injection system includes a funnel and a funnel base, and particles are discharged through a nozzle by gravity. The test tank is 1.0 m high and has an inner diameter of 0.580 m. It is made of a transparent acrylic cylinder for visualization. This experiment used simulant particles, 2 mm in diameter and 2 mm in height, made of stainless steel 304 with a density of approximately 8,000 kg/m^3. The free-fall distance of the particles from the nozzle exit to the free surface of the melt pool was 95 mm, and the distance from the free surface to the particle catcher plate was 0.76 m. The particle discharge rate was approximately 0.10 kg/s.

Fig. 1. The DAVINCI facility [1][2] (POSTECH)

Table 1. The forces and correlations acting on a particle.

$$\vec{F}_G = \rho_s V_s \vec{g}$$

$$\vec{F}_D = \frac{1}{8}\rho_l \pi d^2 |\vec{v}_l - \vec{v}_s|(\vec{v}_l - \vec{v}_s)\left\{\hat{f}^d(\varepsilon_l, R_{Es})\frac{24}{R_{Es}}\right\}$$

$$C_D = \frac{24}{R_{Es}}\left\{1 + R_{Es}^{0.0964+0.5565\Psi} e^{2.3288-6.4581\Psi+2.4486\Psi^2}\right\} + \frac{R_{Es} e^{4.905-13.8944\Psi+18.4222\Psi^2-10.2599\Psi^3}}{R_{Es} + e^{1.4681+12.2584\Psi-20.7322\Psi^2+15.8855\Psi^3}} \quad (\Psi: \text{sphericity})$$

$$\hat{f}^d(\varepsilon_l, R_{Es}) = \frac{C_D}{24} R_{Es} \varepsilon_l^{-\chi}$$

$$\chi = 3.7 - 0.65 e^{-0.5(1.5-\log_{10} R_{Es})^2}$$

$$\vec{F}_L \approx \frac{1}{8}(C_{L\omega} + C_{L\Omega})\rho_l \pi d_s^2 |\vec{u}_s - \vec{u}_l|^2 \frac{(\nabla \times \vec{u}_l)\times \vec{u}_l}{|(\nabla \times \vec{u}_l)\times \vec{u}_l|}$$

$$C_{L\omega} = \begin{cases} \frac{18}{\pi^2}\left(\frac{S_r}{R_{Es}}\right)^{1/2} J(\varepsilon) - \frac{11}{8} S_r e^{-0.50 R_{Es}} & (R_{Es} \le 50) \\ -0.064 e^{0.525 S_r}\left[0.49 + 0.51 \tanh\left\{5 \log\left(\frac{R_{Es} S_r^{0.08}}{120}\right)\right\}\right] & \end{cases}$$

$$C_{L\Omega} = R_r \begin{bmatrix} 1 - 0.62 \tanh(0.3 R_{Es}^{1/2}) \\ -0.24 \tanh(0.01 R_{Es}) \coth(0.8 R_r^{1/2}) \arctan\{0.47(R_r - 1)\} \end{bmatrix}$$

$$\vec{F}_P = -V_s \nabla p$$

$$\vec{F}_V = \varepsilon_s \rho_l C_V \left(\frac{D\vec{u}_l}{Dt} - \frac{D\vec{u}_s}{Dt}\right)$$

Table 2. The forces and correlations acting on a bubble.

$$\vec{F}_G = \rho_g V_g \vec{g}$$

$$\vec{F}_D = \frac{1}{8} C_D \rho_l \pi d_g^2 |\vec{u}_l - \vec{u}_g|(\vec{u}_l - \vec{u}_g)$$

$$C_D = C_{D\infty}\left(e^{3.64\varepsilon_g} + \varepsilon_g^{0.864}\right)$$

slightly contaminated system:

$$C_{D\infty,\mathrm{TS}} = \max\left[\min\left\{\frac{24}{R_{Eg}}\left(1 + 0.15 R_{Eg}^{0.687}\right), \frac{72}{R_{Eg}}\right\}, \frac{8}{3}\frac{E_O}{E_O + 4}\right]$$

$$\vec{F}_L = \rho_l V_g C_L(\vec{u}_l - \vec{u}_g)\times(\nabla \times \vec{u}_l)$$

$$C_L = \begin{cases} \min\left\{0.288 \tanh(0.121 R_{Eg}), f(E_O^H)\right\} & E_O^H < 4 \\ f(E_O^H) & 4 \le E_O^H < 10 \\ -0.27 & 10 \le E_O^H \end{cases}$$

$$f(E_O^H) = 0.00105 E_O^{H3} - 0.0159 E_O^{H2} - 0.0204 E_O^H + 0.474$$

$$E_O^H = E_O\left(1 + 0.163 E_O^{0.757}\right)^{2/3}$$

$$\vec{F}_P = -V_g \nabla p$$

$$\vec{F}_V = \varepsilon_g \rho_l C_V \left(\frac{D\vec{u}_l}{Dt} - \frac{D\vec{u}_g}{Dt}\right)$$

$$\vec{F}_W = \left(\frac{2\rho_l V_g}{d_g}\right)\left(\frac{d_g}{2y}\right)^2 C_W \left|(\vec{u}_l - \vec{u}_g)\vec{k}\right|^2 \vec{n}_W$$

$$C_W = \begin{cases} e^{-0.933 E_O + 1.79} & 1 \le E_O < 5 \\ 0.007 E_O + 0.04 & 5 \le E_O < 33 \end{cases}$$

Fig. 2. The simulant particles in DAVINCI experiment

Two scenarios were used in this experiment: QPC (quiescent pool conditions) without bubble generation, and TPC (two-phase conditions) with bubble-induced natural convection caused by air injection. Most test procedures are identical for both QPC and TPC conditions, except for the air injection section.

The experiment consisted of five steps. Using the particle layer formed in the previous step as the initial condition for the next step, each step involved dropping 1 kg of simulant particles over approximately 10 seconds. To simulate vapor generation from the decay heat of the debris layer, the PCP module contained 32 air chambers with controlled airflow rates. Each chamber was connected to a 40 mm × 40 mm square grid with 16 evenly spaced 1.5 mm-diameter holes. The airflow rate injected into each step was determined by the amount of precipitated debris serving as a heat source due to corium decay.

Fig. 2 depicts the shape of the simulant particles used in the experiment; and Fig. 3 illustrates the air-flow rate injection conditions at each step of the experiment.

According to KIM et al., the following assumptions were used in this experiment: First, the water depth was sufficiently deep, and the melt jet diameter was relatively small, allowing complete fragmentation of the corium melt jet. Second, vapor generation due to phase change within the debris layer was estimated based on volumetric decay heat, assuming that the decay heat of the corium particles was the only source. In other words, natural convection caused by decay heat was not considered. Third, particle remelting was not taken into account. Finally, although bubbles can flatten the existing debris layer over a relatively long period, self-leveling was ignored. [1][2]

3. Numerical method

3.1 Liquid phase

We implemented the MPS method proposed by Koshizuka et al. for analyzing the continuous phase. MPS [5] uses a semi-implicit algorithm to calculate the pressure field by solving the Poisson Pressure Equation (PPE), ensuring incompressibility and stability of the fluid. To account for turbulence, we incorporated the Subgrid-scale turbulence model for Large-eddy simulation of MPS introduced by Gotoh et al., the wall model proposed by Arai et al., and the Contoured Continuum Surface Force model by Duan et al. to compute surface tension forces. The Polygon Wall method proposed by Harada et al. and Zhang et al. was utilized to generate only the surface mesh of a complex wall surface from CAD data, using it directly as a boundary condition.

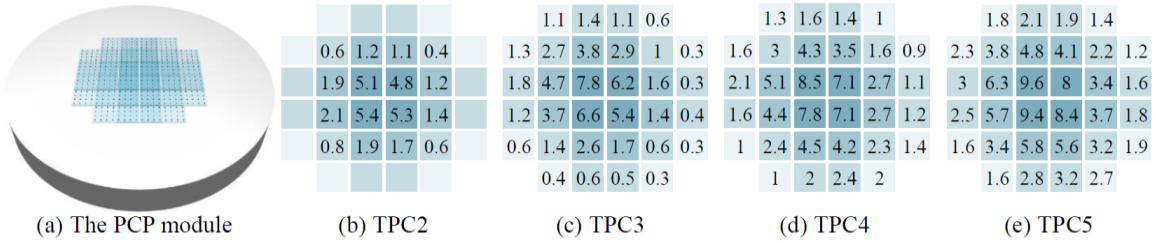

Fig. 3. Distribution of local bubble generation rate reflecting the local volume of the debris bed in growth at each stage (in the DAVINCI experiment)

Table 3. Bubble generation rate in this study

		TPC2	TPC3	TPC4	TPC5
		air flow rate per cell [lpm]			
cell A	4 EA	5.15	6.5	7.625	8.85
cell B	8 EA	1.5625	2.8	3.925	4.925
cell C	12 EA	0.2	1.0833	1.8917	2.625
cell D	8 EA	0	0.6125	1.275	1.8125
total air flow rate [lpm]		35.5	66.3	94.8	120.8

3.2 Solid phase

The discrete element method is a numerical approach for analyzing the behavior of numerous solid particles and their interactions. This technique is a Lagrangian method that solves the six-degree-of-freedom equations of motion, determining each particle's movement by considering all applied forces. The equations of motion are integrated over time using an explicit method with a small time step.

In the discrete element method, a nonlinear viscoelastic model based on the Hertz-Mindlin contact force model is used to calculate collisions between particles and between particles and walls. The following equation describes the external force acting on a particle.

$$\vec{F}_{s,ext} = \vec{F}_G + \vec{F}_D + \vec{F}_L + \vec{F}_P + \vec{F}_V + \vec{F}_T \quad (1)$$

Each of these forces is assumed to be independent and uncoupled from the others. Detailed expressions of these forces are presented in Table 1.

When a particle is surrounded by multiple particles, their influence must be considered when calculating the drag force. To account for the swarm effect on the drag coefficient, a dimensionless correlation for the liquid volume fraction is used. In this study, the Di Felice correlation, effective for high- and low-density particle flows and widely used for spherical and non-spherical particles, was employed. Additionally, the Haider and Levenspiel correlation was used to account for the drag force of non-spherical particles.

To account for particle lift, we used the correlation proposed by Shi and Rzehak, and adopted the method proposed by Sato et al. for the particle/bubble-induced turbulence model. The total viscosity of the liquid was calculated as the sum of molecular viscosity, eddy viscosity due to turbulence, and viscosity induced by particles and bubbles. Turbulent dispersion of the disperse phase was computed using the method proposed by Ermak et al.

3.3 Gas phase

When dealing with multiple bubbles, such as in bubble columns, two methods have been proposed based on how the dispersed phase is handled. The first uses a grid-based Eulerian approach for both the continuous and dispersed phases (E-E). The second combines the Eulerian method for the continuous phase with the Lagrangian method for the dispersed phase (E-L).

The E-E model describes the time-dependent motion of both phases using volume-averaged mass and momentum conservation equations. Bubbles within the computational cell are represented by their volume fractions. In contrast, the E-L model adopts a continuum description of the liquid phase and tracks each bubble using Newtonian equations of motion. This enables direct consideration of additional effects related to bubble-bubble and bubble-liquid interactions. Unlike the E-E model, the E-L model does not need an additional model to predict bubble size distribution.

However, it is important to note that numerical diffusion can still occur in continuous-phase calculations even when using the E-L method. To address this, we adopted an approach that removes numerical diffusion from the two-phase analysis by introducing a Lagrangian analysis of the continuous phase.

The DBM method, which employs the Lagrangian approach to analyze bubbles, was first introduced by Delnoij et al. [6]. Each bubble is tracked according to the following equation of motion.

$$\rho_g V_g \frac{d\vec{u}_g}{dt} = \vec{F}_{g,ext} \quad (2)$$

$$\vec{F}_{g,ext} = \vec{F}_G + \vec{F}_D + \vec{F}_L + \vec{F}_P + \vec{F}_V + \vec{F}_T + \vec{F}_W \quad (3)$$

Each of these forces is assumed to be independent and uncoupled from the others. Detailed expressions of these forces can be found in Table 2. Based on the terminal rising velocity of a bubble, many researchers, including Ishii, Zuber, and Tomiyama, expressed the drag coefficient of the bubble as a function of the

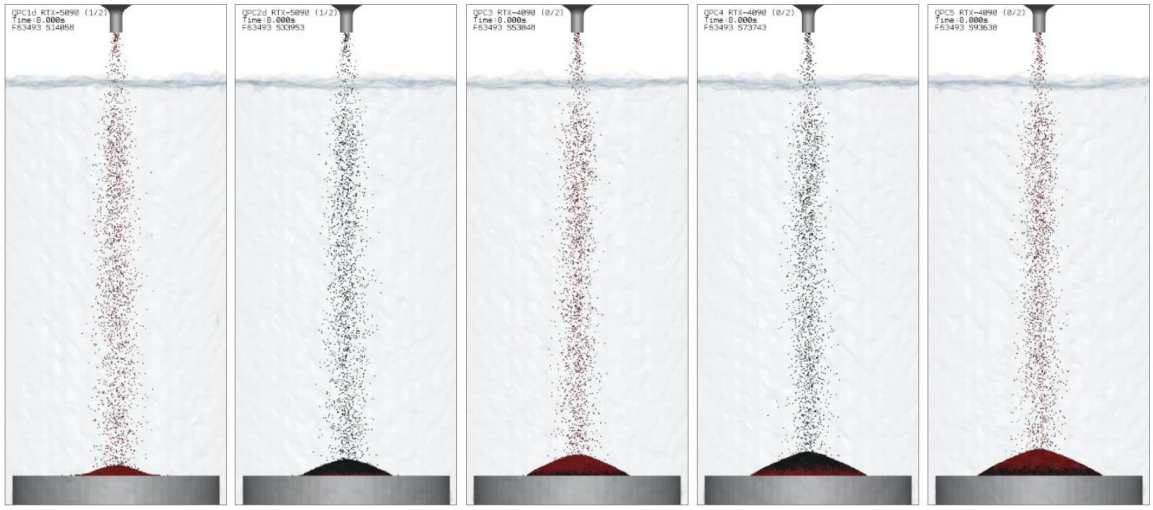

(a) QPC1 (b) QPC2 (c) QPC3 (d) QPC4 (e) QPC5

Fig. 4. Snapshots of the simulation at each stage according to the gap-tooth approach. (QPC, sphericity 0.874)

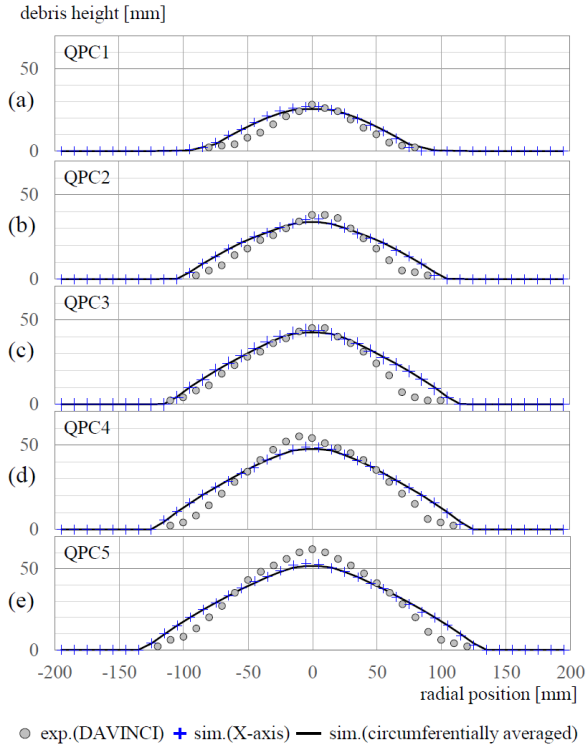

Fig. 5. Comparison of the debris bed at each stage (sphericity 0.874)

Reynolds number and the Eö number. In this study, Tomiyama's model (slightly contaminated system) was adopted for drag coefficient calculation, and Rusche's model, which uses the volume fraction around the bubble as a function to consider the effect of interaction between neighboring bubbles, was used.

To account for the lift force acting perpendicular to the relative motion between the bubble and the fluid, Tomiyama's lift coefficient correlation was used. The wall-effect force acting on the bubble moving near the wall and the turbulence dispersion of the dispersed phase, as proposed by Ermak et al., were considered.

3.4 Interphase coupling

The unresolved approach uses a length scale for the continuous phase that is similar to or larger than that of the dispersed phase and employs empirical correlations to determine the force transmitted between the two phases. This method is suitable for analyzing the interaction behavior of many particles or bubbles over a relatively large domain. Essentially, the unresolved approach solves the Navier-Stokes equations with a local averaging technique for analyzing the continuous phase. In this study, for accurate volume fraction calculation using the gridless particle-based method, the approach of directly calculating the volume defined by the overlap between the virtual sphere, defined by the coupling radius, and an arbitrary sphere was used. [7]

4. Numerical analysis

The code was written in the CUDA v12.8 environment to run on GPUs such as Nvidia RTX 4090 or RTX 5090. Four Cell-Linked Lists (CLL) were used to enable all particles defining each phase to quickly and efficiently search for their neighbors.

Before the simulations, the following process was performed. In the first step, we modeled a tank with conditions identical to the experiment and generated MPS particles to analyze the liquid. After generating the particles, the simulation was performed for a sufficient amount of time until the motion caused by interactions was stabilized.

To generate bubbles for each condition within the stabilized liquid from the previous step, 512 seed points were defined at the same locations as in the experiment,

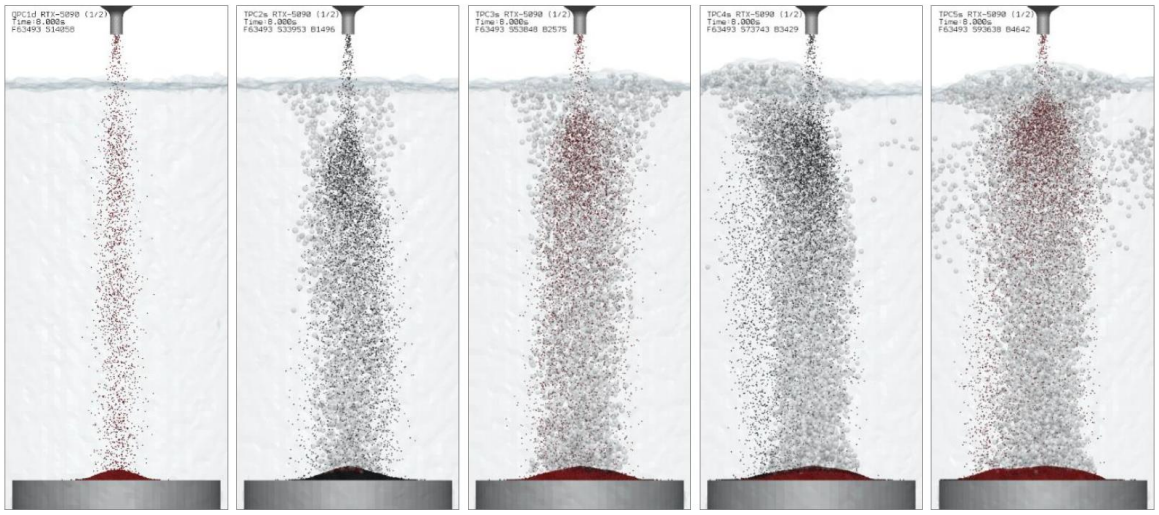

(a) QPC1 (b) TPC2 (35.5 lpm) (c) TPC3 (66.3 lpm) (d) TPC4 (94.8 lpm) (e) TPC5 (120.8 lpm)

Fig. 6. Snapshots of the simulation at each stage according to the gap-tooth approach. (TPC, sphericity 0.874)

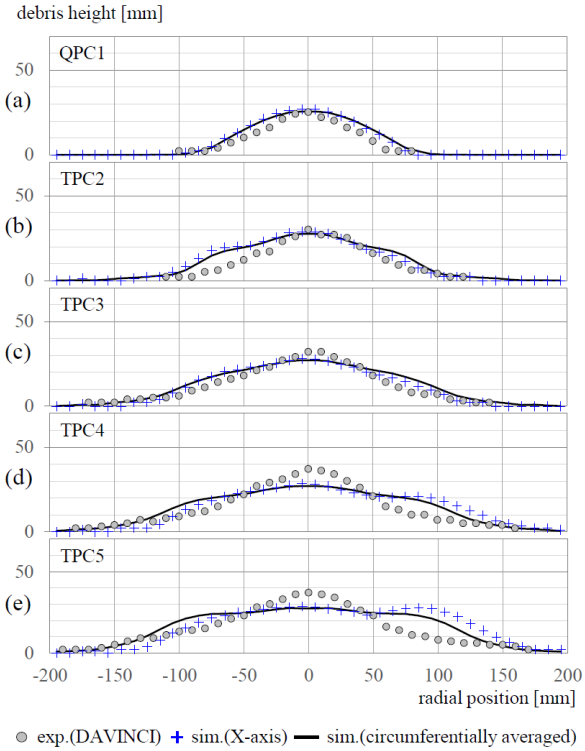

Fig. 7. Comparison of the debris bed at each stage (sphericity 0.874)

and bubbles were generated at appropriate time intervals based on the number of bubbles produced per unit time. To control the bubble generation rate, the number of bubbles produced from each seed was recorded over a long period, and bubble creation was regulated so that each seed generated a specific number of bubbles. The calculations were performed for 120 seconds to ensure the bubble column and flow field were fully developed.

According to Kim et al. [1][2], the average bubble size measured at the center, when converted to an equivalent volume diameter, was 10.2 mm, with a standard deviation of 1.45 mm. In this study, bubbles with diameters ranging from 8 mm to 12 mm were generated.

5. Results

5.1 QPC (Quiescent Pool Conditions)

Simulation was conducted under QPC conditions without bubble generation. Similar to the experiment, the analysis consisted of five steps. Each step used the particle layer generated in the previous step as the initial condition, and each step was configured to drop 1 kg of simulant particles for approximately 10 seconds.

Fig. 4 shows snapshots taken at 8 seconds of each step and the final debris bed. Most particles fell vertically in narrow cylindrical columns, while some particles were scattered due to turbulence and collisions. The particles reached a narrow region above the PCP, and the particle layer grew rapidly as they accumulated.

Fig. 5 presents cross-sectional profiles along the particle bed centerline and circumferentially averaged profiles to reflect the debris bed geometry at the end of each step. Compared with the results reported by Kim et al., the maximum bed heights were slightly lower, and the radial widths were slightly larger for QPC4 and QPC5. The increase in radial width is due to particles rolling down from the central region.

5.2 TPC (Two-phase Conditions)

Table 3 shows the simulation conditions for implementing the same air flow rate across four different cell types, categorized by their distance from the PCP center, to reflect the step-by-step air flow rate injection conditions shown in Fig. 3. The air flow rates

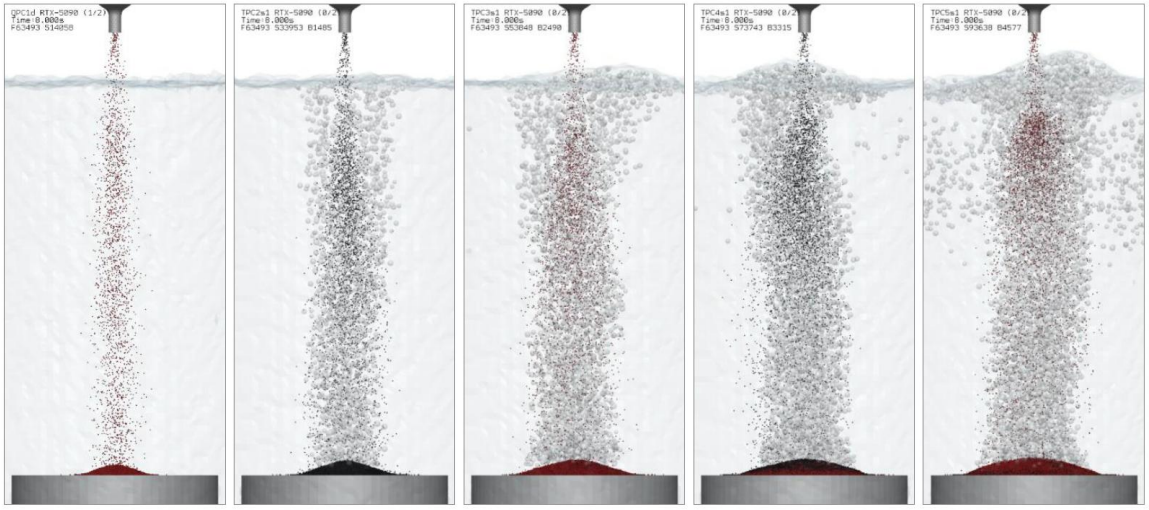

(a) QPC1 (b) TPC2 (35.5 lpm) (c) TPC3 (66.3 lpm) (d) TPC4 (94.8 lpm) (e) TPC5 (120.8 lpm)

Fig. 8. Snapshots of the simulation at each stage according to the gap-tooth approach. (TPC, sphericity 1.0)

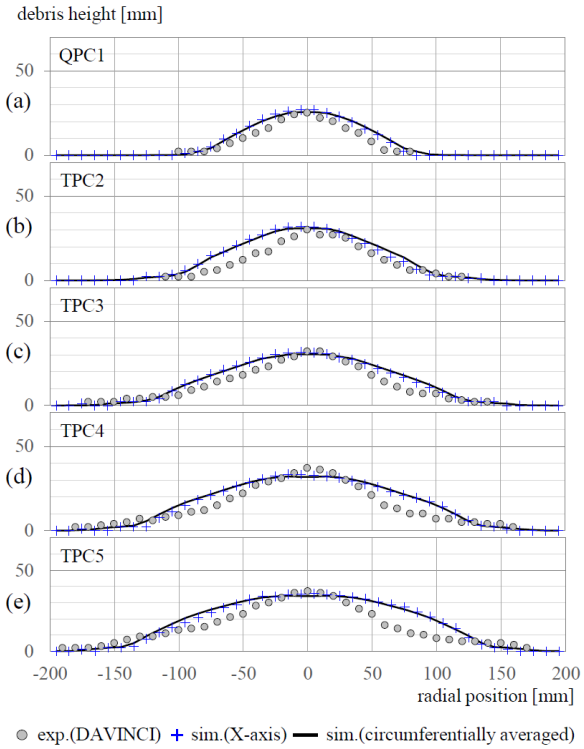

Fig. 9. Comparison of the debris bed at each stage (sphericity 1.0)

used to generate bubbles were 35.5 lpm, 66.3 lpm, 94.8 lpm, and 120.8 lpm for TPC2 through TPC5, respectively. In this simulation, air was injected for 15 seconds, then stopped, and the calculation was continued until all particles in the water settled at the bottom.

Fig. 6 displays snapshots captured at 8 seconds for each TPC step, along with the final debris bed images. In the TPC test, the upward bubble stream caused an upward flow of liquid, which collided with the downward particle stream. This interaction influenced the particle trajectories, reducing sedimentation in the central region of the PCP. As a result, the particle bed height increased more slowly and became more dispersed over a wider area compared to the QPC at the same step.

Fig. 7 presents the cross-sectional profile along the particle bed centerline and the circumferentially averaged profile, illustrating the shape of the debris bed at each step's end. Compared to the results from the experiment by Kim et al., the maximum height in the central region was slightly lower in TPC4 and TPC5.

The simulant particles used in Kim et al.'s experiments were cylindrical, with equal height and diameter, resulting in a sphericity of 0.874 and a higher drag coefficient than that of a perfectly spherical particle. Thus, a perfectly spherical particle (sphericity of 1.0) has a lower drag coefficient, which creates a disadvantageous condition for the coolability of the debris bed. Consequently, this study also conducted the same simulations at a sphericity of 1.0, with the results shown in Figures 8 and 9.

Comparing Figures 6 and 8, the lower drag coefficient makes the particle less sensitive to the upward flow induced by the bubble, thereby reducing particle dispersion. Comparing Figures 7 and 9, it is evident that the central height of the debris bed decreases slightly due to a decrease in the drag coefficient caused by increased sphericity, and radial particle dispersion is also slightly reduced. This condition is disadvantageous for the coolability of the debris bed.

Fig. 10 compares the shapes of the final debris beds obtained at each step. As previously mentioned, the TPC results show that, compared to the QPC at the same step, the particle layer height increases more slowly and is more widely distributed. Due to the

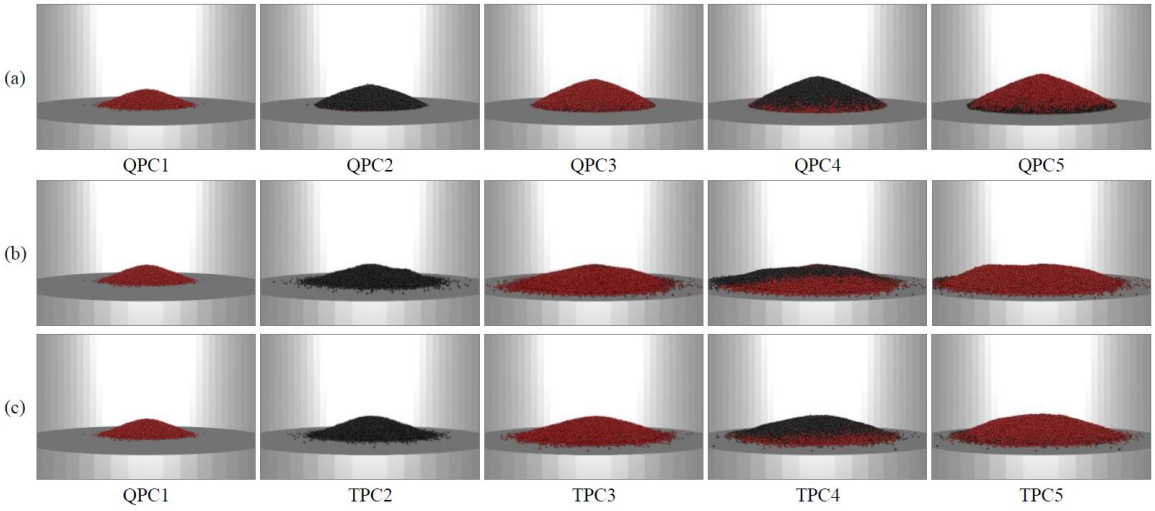

Fig. 10. Results of the simulation at each stage according to the gap-tooth approach.
(a) QPC (b) TPC, sphericity 0.874 (c) TPC, sphericity 1.0

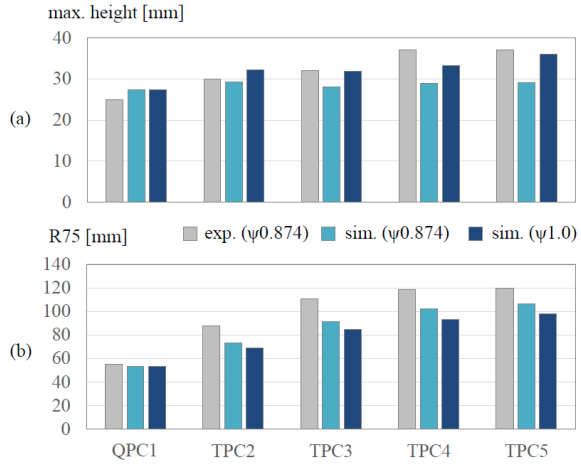

Fig. 11. Comparison of the debris bed shape at each stage
(a) the maximum height (b) the R75

reduced drag coefficient caused by increased sphericity, particles are slightly more likely to be deposited in the center, and their radial dispersion is decreased.

Kim et al. defined the radius from the center of the PCP as the radius that contains 75% of the total debris volume, a measure of radial particle dispersion denoted R75. Fig. 11 compares the maximum height of the debris bed and R75 at each step for two sphericities. Compared to the experimental results, the simulation results show that the maximum height and R75 at the center are slightly lower for both sphericities. It is presumed that some differences between the experiment and the simulations occurred due to differences in friction and particle-particle collisions, as well as differences in bed porosity, since the simulated particles were cylindrical in the actual experiment, whereas they were spherical in the simulations.

The difference between the experimental and simulation results can also be explained by the following reasons. First, this study did not consider bubble aggregation or bubble splitting. It is expected that when rising bubbles collide with descending particles, large bubbles will split into smaller ones, and under certain conditions, two rising bubbles will regenerate into a single bubble. However, research on this phenomenon remains insufficient, and although some researchers have attempted numerical analysis, no clear model has yet been established. Second, the drag and lift calculated for dispersed phases, such as bubbles and particles, are steady-state forces, and unsteady-state forces were not considered. Research on these unsteady forces is also insufficient; they have not yet been established or require significant memory and computation for numerical implementation.

Furthermore, while the experiment was conducted under strictly controlled conditions, some degree of uncertainty is inevitable in the results. In particular, bubbles measured at the center of the bubble column are non-spherical (flattened ellipsoids), and under these conditions, the upward trajectory of a single bubble becomes unstable. The causes are known to include the continuous shape instability of bubbles, the wake induced by rising bubbles, and contaminants in the liquid affecting the bubble surface. This affects the flow field and ultimately leads to uncertainty in the downward trajectory of particles. The difference between experimental and numerical analysis results must be understood by accounting for the uncertainty of the phenomenon and the limitations of numerical analysis mentioned above.

6. Conclusions

In an unresolved method, we coupled MPS, DEM, and DBM using a fully Lagrangian approach to simulate the collision of the bubble column generated by air injection with the particle column formed by falling debris particles. The quantitative measurement

results obtained in the DAVINCI experiment were directly compared with the simulation results. Although there is significant uncertainty in experiments and simulations due to the complex behavior of many bubbles and particles resulting from numerous collisions and the resulting fluid flow, the simulation results showed similar trends to the experiments.

The simulations were conducted under two conditions (sphericity 0.874 and 1.0) using the gap-tooth method in five steps, with QPC and TPC conditions, respectively. In the TPC test, the upward-moving bubble stream caused an upward flow of liquid and collided with the descending particle stream. This influenced the particle trajectories and suppressed sedimentation in the central area of the PCP. Consequently, the debris bed height increased more slowly and was spread over a larger area compared to the QPC test. At a sphericity of 1.0, the low drag coefficient made the particle less sensitive to the bubble-induced upward flow, thereby reducing particle dispersion. This is a disadvantageous condition for the coolability of the debris bed.

Even though the experiment was conducted under strictly controlled conditions, the results are expected to have some uncertainty.

According to Kim et al. [2], the bubbles measured at the center of the bubble column were non-spherical (flattened ellipsoids), and in these conditions, a single bubble's rising trajectory becomes unstable. It is known that this instability is caused by the continuous shape instability of the bubble, the wake induced by the rising bubble, and contaminants in the liquid that affect the bubble surface. This is distinguished separately from the lift caused by the velocity gradient. Due to this rising trajectory instability, the bubble's path becomes uncertain, which affects the flow field and ultimately leads to uncertainty in the particle's falling trajectory.

The following limitations are noted in the numerical analysis. First, coalescence and bubble breakup were not considered in this study. When a rising bubble and a falling particle collide, it is expected that a large bubble will break into smaller bubbles and that two rising bubbles will merge into one under certain conditions. However, research on this phenomenon is still limited, and although some researchers have attempted numerical analysis, no clear model has yet been established. Second, the drag and lift forces calculated for dispersed phases, such as bubbles and particles, are steady forces, and unsteady forces are not considered. Research on these unsteady forces is also limited, and modelling or numerical implementation requires substantial memory and computational resources.

The differences between the experimental and numerical results should be understood by considering the uncertainties of the phenomena and the limitations of the numerical analysis described above.

REFERENCES

[1] E. Kim, M. Lee, H. Park, K. Moriyama, and J. Park, Development of an ex-vessel corium debris bed with two-phase natural convection in a flooded cavity, Nuclear Eng. and Design, Vol. 298, pp. 240-254, 2016.

[2] E. Kim, Debris Bed Formation during Ex-Vessel Severe Accidents in Light Water Reactors, Doctoral Thesis, Pohang University of Science and Technology, 2016.

[3] Y. Son, I. Seo, and C. Ahn, Fully Lagrangian Approach of Three-Phase Systems for Debris Bed Formation (Part I: DAVINCI experiment), Trans. of the Korean Nuclear Soc. Spring Meeting, 2025.

[4] Y. Son, I. Seo, and C. Ahn, Fully Lagrangian Approach of Three-Phase Systems for Debris Bed Formation (Part II: Effect of Sphericity), Trans. of the Korean Nuclear Soc. Spring Meeting, 2025.

[5] S. Koshizuka, K. Shibata, M. Kondo, and T. Matsunaga, Moving Particle Semi-Implicit Method, Academic Press, 2018.

[6] E. Delnoij, J.A.M. Kuipers, and W. Van Swaaij, A three-dimensional CFD model for gas–liquid bubble columns. Chem. Eng. Sci., Vol. 54, pp. 2217–2226, 1999.

[7] Y. Son, C. Ahn, S. Lee, Using a Lagrangian-Lagrangian Approach for Studying Flow Behavior Inside a Bubble Column, Nuclear Eng. and Tech., Vol. 55, pp. 4395-4407, 2023.